

# Nano-confining Red Phosphorus in a Carbon Hierarchical Superstructure for Superior Potassium Storage

Zibin Liang<sup>+, [a, b]</sup> Tianjie Qiu<sup>+, [a, b]</sup> Jinqian Cheng,<sup>[a, b]</sup> Yanqun Tang,<sup>[a, b]</sup> Yingxiao Wu,<sup>[a, b]</sup> Jinming Shi,<sup>[a, b]</sup> Song Gao,<sup>\*[a, b]</sup> and Ruqiang Zou<sup>\*[a, b]</sup>

High-capacity red phosphorus is a promising candidate for anode material of potassium-ion batteries while the poor electrical conductivity and large volume variation may cause severe material pulverization and performance deterioration during cycling. Incorporation of red phosphorous with porous carbon substrates is a potential strategy to solve these issues, which can spatially confine the phosphorus particles and promote mass/charge transfer processes. Herein, a hierarchical nitrogen-doped microporous carbon superstructure derived from nanorod-assembled metal-organic framework superstructure was presented to confine red phosphorus (P@NCS) for potassium storage. Remarkably, P@NCS as an anode material

demonstrated a high reversible specific capacity of 551 mAh g<sup>-1</sup> at 0.1 A g<sup>-1</sup> after 100 cycles along with a high initial Coulombic efficiency of 76%. Control experiments and theoretical calculations verified that the excellent potassium storage performance was attributed to the strong confinement effect of the nitrogen-doped micropores and the unique nanorod-assembled superstructure. Furthermore, a potassium-ion full cell was assembled using P@NCS and 3,4,9,10-perylenetetracarboxylic dianhydride as anode and cathode material respectively, demonstrating the great potential of P@NCS for practical potassium-ion batteries.

## 1. Introduction

The development of high-performance energy storage systems is essential to power our society in an environmentally friendly and sustainable way.<sup>[1,2]</sup> Lithium-ion batteries (LIBs), which have been widely used to power the portable electronics and electric vehicles, represent one of the most promising classes of electrochemical energy storage devices.<sup>[3,4]</sup> However, the high cost, uneven distribution, and limited availability of lithium resources greatly hinder the development of LIBs for large-scale and low-cost energy storage.<sup>[5]</sup> Recently, potassium-ion batteries (PIBs) have attracted great attention as alternatives to LIBs in virtue of the low standard reduction potential, high abundance, and low cost of potassium.<sup>[6–10]</sup> Searching electrode materials with excellent electrochemical properties is crucial to improve the energy density and cycling stability of PIBs. Recently, alloy-type materials (e.g., phosphorus, Sn, Bi, and Sb) have been explored as promising anode materials for PIBs,

which could provide high specific capacity through an alloying/dealloying process.<sup>[11–15]</sup> Particularly, phosphorus-based materials have recently attracted numerous interests in virtue of their high theoretical specific capacity (1154 mAh g<sup>-1</sup> for K<sub>4</sub>P<sub>3</sub>), desirable voltage platform, low cost, and high abundance.<sup>[16,17]</sup> However, two dominant problems are essential to be solved prior to the widespread use of phosphorus-based anode materials for PIBs: i) the electric conductivity of red phosphorus is low, resulting in low utilization efficiency and low rate capability; ii) there is a large volume change of phosphorus particles during potassiation/depotassiation cycles, leading to the pulverization of phosphorus particles and thus poor cycling stability.<sup>[18–20]</sup>

In addition, it has been demonstrated that graphite, which is a dominating anode material for LIBs, can also store potassium by intercalation of potassium ions with desirable specific capacity.<sup>[21–23]</sup> But the rate capability and cycling stability of graphite for PIBs are poor due to the sluggish potassium reaction/diffusion kinetics and large volume change during cycling. Recent progresses have demonstrated that fabrication of nanocarbon materials such as carbon nanofibers and carbon nanosheets could boost the potassium ion storage and render excellent cycling efficiency of PIBs.<sup>[24,25]</sup> Moreover, construction of three dimensional (3D) porous carbon materials with hierarchical porosity, defects, heteroatom doping, and short-range ordered graphitic regions could lead to much improved rate capability and cycling stability, which can be attributed to the shortened potassium ion diffusion pathway and enhanced potassium ion storage ability.<sup>[26–29]</sup> However, the use of these high-surface area carbon materials always causes many issues such as low initial Coulombic efficiency, unapparent voltage platform, and low volumetric energy density, which

[a] Dr. Z. Liang,<sup>+</sup> T. Qiu,<sup>+</sup> J. Cheng, Y. Tang, Y. Wu, J. Shi, Dr. S. Gao, Prof. R. Zou

*Beijing Key Laboratory for Theory and Technology of Advanced Battery Materials*

*School of Materials Science and Engineering*

*Peking University*

*Beijing 100871, China*

*E-mail: rzou@pku.edu.cn*

*gaosong198600@pku.edu.cn*

[b] Dr. Z. Liang,<sup>+</sup> T. Qiu,<sup>+</sup> J. Cheng, Y. Tang, Y. Wu, J. Shi, Dr. S. Gao, Prof. R. Zou

*Institute of Clean Energy*

*Peking University*

*Beijing 100871, China*

[+] These authors contributed equally to this work.

 Supporting information for this article is available on the WWW under <https://doi.org/10.1002/batt.202100264>

would lead to severe active material loss and unstable output voltage.

Taking the aforementioned factors into consideration, combination of carbon materials and phosphorus may be a win-win strategy to achieve an optimal potassium storage performance. The incorporation of phosphorus components into the pores/defects of carbon materials can not only enhance the specific capacity and enable a stable voltage platform, but also reduce the surface area of carbon materials and thus hinder their side reaction with electrolytes, resulting in a high initial Coulombic efficiency. Besides, the carbon substrates can greatly improve the electrical conductivity and provide space to buffer the volume change during potassiation/depotassiation cycles. Moreover, carbon substrates can induce the formation of nano-sized phosphorus particles, which shortens the potassium ion diffusion pathways and improves the potassium storage kinetics.

Herein, we developed a nitrogen-doped microporous carbon superstructure (NCS) to confine red phosphorus (P@NCS) as a high-performance anode material for PIBs. NCS was fabricated by pyrolysis of a sacrificed nanorod-assembled metal-organic framework (MOF) superstructure. The confinement of red phosphorus within the nitrogen-modified micropores enabled a reversible and fast alloying reaction between phosphorus and potassium as the micropores as well as the carbon superstructure can buffer the volume change of phosphorus during cycles and facilitate the electron and mass transport. Benefiting from these advantages, the resultant P@NCS with optimized phosphorus loading delivered a high reversible specific capacity of  $551 \text{ mAh g}^{-1}$  at  $0.1 \text{ A g}^{-1}$  after 100 cycles along with a high initial Coulombic efficiency of 76%. Moreover, a high specific capacity of  $271 \text{ mAh g}^{-1}$  at  $1 \text{ A g}^{-1}$  after 500 cycles was recorded, revealing a high cycling stability of the P@NCS. A potassium-ion full cell was also constructed using the P@NCS and 3,4,9,10-perylenetetracarboxylic dianhydride (PTCDA) as anode and cathode materials, respectively, which can lighten a blue light-emitting diode (LED) with working voltage higher than 2.5 V. Theoretical calculations and control experiments demonstrated that the outstanding potassium storage performance of the P@NCS was attributed to the synergism of the nitrogen-modified micropores and the highly dispersed red phosphorus components within these micropores. This work not only provided a high-performance anode material for PIBs, but also offered experimental basis and theoretical guidance for design and fabrication of phosphorus/carbon composites with high initial Coulombic efficiency, high capacity, high rate capability, and high cycling stability for electrochemical energy storage.

## 2. Results and Discussion

The synthetic process of P@NCS was schematically illustrated in Figure 1(a). Al-based metal-organic framework (Al-MOF) with nanorod-assembled superstructure, which could be simply fabricated through a one-pot solvothermal synthesis, was used as the sacrificial precursor to fabricate nitrogen-doped carbon

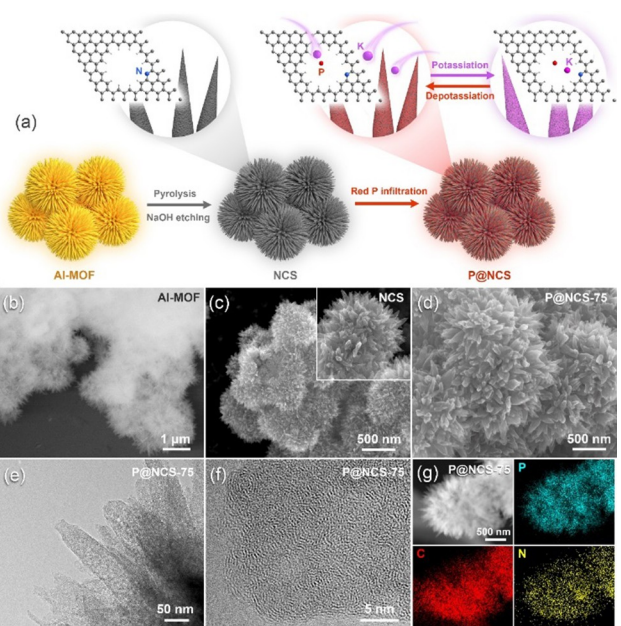


**Figure 1.** a) Schematic illustration of the synthetic process of P@NCS. b) SEM image of Al-MOF nanorod-assembled superstructure. c) SEM images of the NCS derived from the Al-MOF superstructure. d) SEM, e,f) TEM, g) HAADF-STEM image and corresponding EDS profiles of P@NCS-75.

superstructure (NCS) (Figure 1b). After pyrolysis of Al-MOF and Al removal by NaOH washing, highly porous NCS with hierarchical superstructure morphology inheriting from MOF precursor was obtained (Figures 1c and S1).<sup>[28]</sup> Then, red phosphorus was introduced into the NCS by an evaporation-condensation method at 600 °C. During this evaporation-condensation process, red phosphorus was evaporated and infiltrated within the pores of NCS. The loading of red phosphorus could be facilely adjusted by mixing different weights of red phosphorus with NCS (the resultant composites were named as NCS-X, X represents 50, 75, and 100 mg of red phosphorus, respectively), which were quantified by thermogravimetric analysis (Figure S2). Scanning electron microscope (SEM) images demonstrated that P@NCS-75 retained the nanorod-assembled superstructure after red phosphorus infiltration without isolated red phosphorus particles (Figure 1d). Transmission electron microscope (TEM) images also indicated the absence of large red phosphorus particles in low-loading P@NCS-75, which can be attributed to the excellent confinement effect of the micropores of NCS (Figure 1e–f). The uniform distribution of the red phosphorus component was also revealed by high-angle annular dark-field scanning (HAADF-STEM) image and the corresponding energy-dispersive X-ray spectroscopy (EDS) images (Figure 1g). However, when increasing red phosphorus loading as high as P@NCS-100, aggregated red phosphorus particles were observed (Figure S3), which could be attributed to the complete occupation of micropores leading to excess isolated red phosphorus particles.

X-ray diffraction (XRD) patterns of all P@NCS samples displayed broad peaks at about 15.5°, which can be assigned to the characteristic peak of red phosphorus (Figure 2a).<sup>[17,30]</sup> The

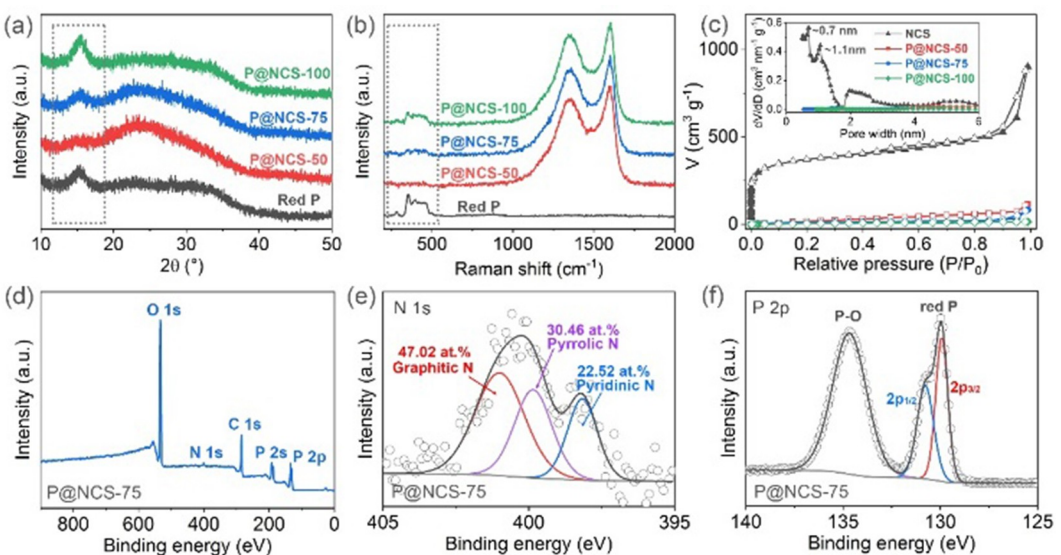


**Figure 2.** a) XRD patterns, b) Raman spectra, c) nitrogen sorption isotherm and corresponding pore size distribution of P@NCS. d) Full XPS spectrum, e) high-resolution N 1s spectrum, and f) high-resolution P 2p spectrum of P@NCS-75.

intensity of these characteristic peaks increased as the loading of red phosphorus increased. Similarly, Raman profiles of P@NCS showed characteristic peaks of red phosphorus, while the intensity of these peaks increased along with the increase of red phosphorus loading, suggesting the successful loading of red phosphorus by NCS (Figure 2b). Nitrogen sorption measurement at 77 K was carried out to reveal the pore structure of P@NCS (Figure 2c). It suggested that NCS possessed a large amount of micropores with pore width of about 0.7 and 1.1 nm. After red phosphorus infiltration, the nitrogen uptake of P@NCS decreased dramatically. P@NCS were nearly nonporous materials with much reduced BET surface areas and none micropores (Table S1), indicating that the pores of NCS were filled with red phosphorus components. It is expected that the abundant micropores of NCS can spatially confine the red phosphorus and enabled the formation of ultrafine red phosphorus species with size smaller than those of the micropores, which is consistent with the TEM results. X-ray photoelectron spectroscopy (XPS) measurements also proved the existence of red phosphorus in P@NCS-75 (Figure 2d). High-resolution XPS spectrum of the N 1s can be divided into three peaks at 401.0, 399.9, and 398.2 eV, which were assigned to graphitic (47.02 at%), pyrrolic (30.46 at%), and pyridinic (22.52 at%) nitrogen, indicating the doping of N into carbon superstructures (Figure 2e).<sup>[28]</sup> The high-resolution XPS spectrum of P 2p showed characteristic peaks of oxidized phosphorus and elemental red phosphorus, suggesting the partial oxidation of red phosphorus (Figure 2f).<sup>[19]</sup> These above-mentioned results manifested the strong confinement effect of NCS, which can effectively confine ultrafine red phosphorus within the N-doped micropores.

The electrochemical performance of P@NCS for PIBs was first evaluated by cyclic voltammetry (CV) measurements with a voltage window from 0 to 3 V (vs. K<sup>+</sup>/K). The anodic peak at about 0.75 V during the first cycle was assigned to the

formation of solid electrolyte interface (SEI) film (Figure 3a). After the first cycle, the CV curves became stable and exhibited three pairs of redox peaks, which were assigned to the stepwise and reversible reaction between red phosphorus and potassium. These reversible reactions were also corresponding to the voltage platforms in galvanostatic charge-discharge (GCD) profiles (Figure 3b). Remarkably, P@NCS-75 displayed a high initial Coulombic efficiency of 76% along with reversible capacity of 666 mAh g<sup>-1</sup> at a current density of 0.1 A g<sup>-1</sup>, which surpassed pure NCS and most of the reported phosphorus-based anode materials for PIBs (Figure S4 and Table S2). The cycling stability at a current density of 0.1 A g<sup>-1</sup> of P@NCS was showed in Figure 3(c), which revealed that the red phosphorus loading played an important role on the electrochemical performance of P@NCS. For P@NCS-100 with high phosphorus loading, despite the high capacity at the beginning, the capacity decreased dramatically and reached only 351 mAh g<sup>-1</sup> after 100 cycles. The capacity fading of P@NCS-100 may be attributed to the existence of large red phosphorus particles that would undergo severe cracking and pulverization. For P@NCS-50 with low phosphorus loading, it possessed a high cycling stability, but its capacity was low at the beginning due to the lack of active phosphorus component. Whereas P@NCS-75 with moderate phosphorus loading exhibited both high capacity and high cycling stability with capacity of 551 mAh g<sup>-1</sup> after 100 cycles, higher than those of NCS, P@NCS-50 and P@NCS-100. For comparison, pure red phosphorus displayed much lower capacity after the second cycle, suggesting the importance of the NCS substrate. The rate capability of P@NCS was also evaluated (Figure 3d). It showed that P@NCS-75 possessed the best rate capability with capacity of 561, 507, 459, 448, 401, 342 mAh g<sup>-1</sup> at current density of 0.2, 0.4, 0.8, 1, 2, 4 A g<sup>-1</sup>, respectively. Even at an ultrahigh current density of 8 A g<sup>-1</sup>, its capacity can remain at 238 mAh g<sup>-1</sup>. The rate capability of P@NCS-75 was higher than those of P@NCS-50

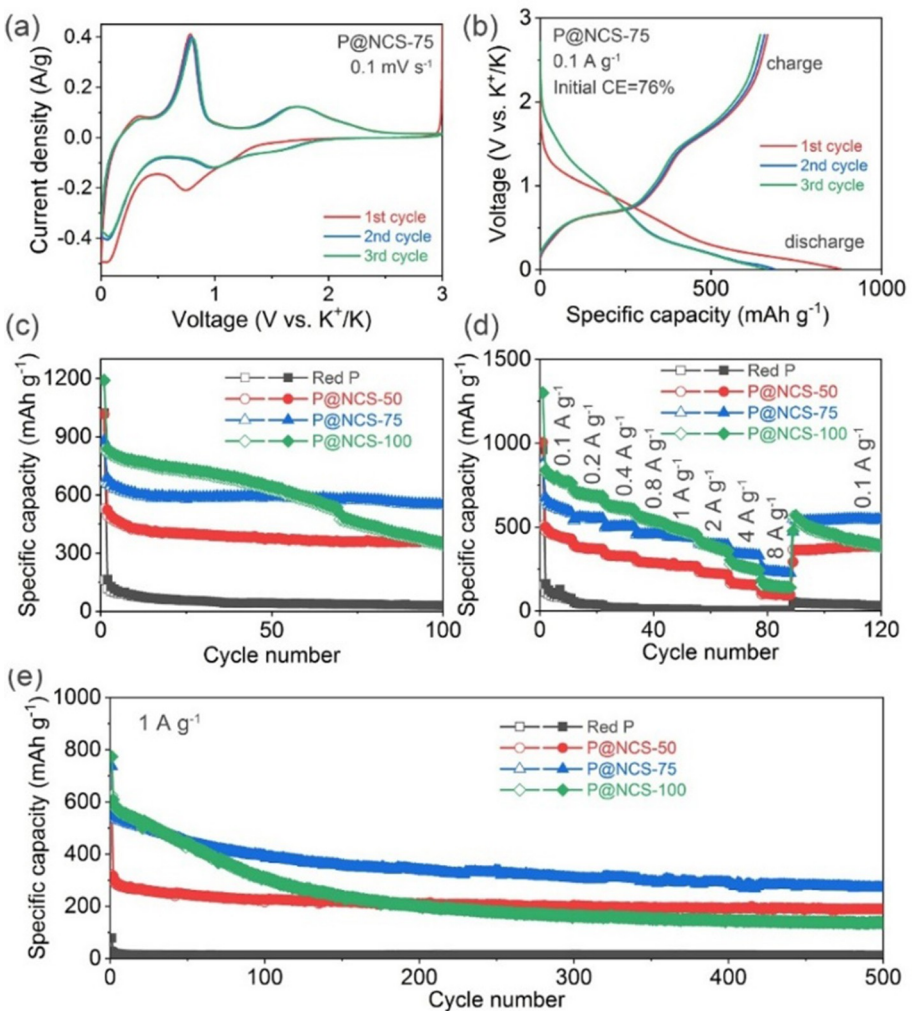


**Figure 3.** a) CV curves and b) GCD profiles at the first three cycles of P@NCS-75. c) Cycling performance of P@NCS at  $0.1 \text{ A g}^{-1}$  over 100 cycles. d) Rate capability of P@NCS at different current densities. e) Cycling performance of P@NCS at  $1 \text{ A g}^{-1}$  over 500 cycles.

and P@NCS-100, indicating that an appropriate phosphorus loading is also essential to achieve a high rate capability. Long-term stability of P@NCS at  $1 \text{ A g}^{-1}$  was displayed in Figure 3(e). It showed that P@NCS-75 had the highest capacity ( $271 \text{ mAh g}^{-1}$ ) after 500 cycles, demonstrating a high cycling stability of P@NCS-75.

To further study the potassium storage behavior of P@NCS-75, galvanostatic intermittent titration (GITT) measurements were carried out. The corresponding potassium ion diffusion coefficient ( $D$ ) exhibited obvious decrease at 0.2 and 1.2 V during the discharge process, while during charging the decrease of  $D$  appeared at 0.7 and 1.5 V. The decrease of  $D$  was corresponding to the stepwise redox reactions of phosphorus and potassium (Figure S5). To investigate the chemical composition of the fully discharged P@NCS-75, XPS and EDS measurements were carried out. XPS survey spectrum demonstrated the existence of abundant potassium and phosphorus in the fully discharged P@NCS-75, while the high-resolution XPS of K 2p and P 2p indicated that the potassium and phosphorus were in the form of potassium phosphate, which may be formed by oxidation of the potassium phosphide product in the air

(Figure S6a–c). EDS profiles also suggested the existence of abundant potassium, which was uniformly distributed in the NCS matrix (Figure S6d). These results demonstrated that the potassium was stored by the reversible stepwise redox reaction of phosphorus and potassium, forming potassium phosphide in the pores of NCS.

To investigate the roles of micropores and nitrogen doping in NCS substrate on the confinement of red phosphorus and potassium storage performance, density functional theory (DFT) calculations were carried and 4 kinds of microporous carbon models with different kinds of nitrogen doping were constructed (microporous carbon models without nitrogen doping, with pyrrolic, graphitic, and pyridinic nitrogen doping, respectively) (Figure 4a). The pore sizes of these models are about  $\sim 0.8 \text{ nm}$ , which is close to that measured by nitrogen sorption ( $\sim 0.7 \text{ nm}$  discussed above). It was calculated that all the four kinds of micropores without nitrogen doping, with pyrrolic, graphitic, and pyridinic nitrogen doping demonstrated negative free energy changes of  $-0.53$ ,  $-0.29$ ,  $-0.73$ , and  $-0.47 \text{ eV}$  after loading red phosphorus within the micropores, which indicated that the micropores possessed strong confinement.

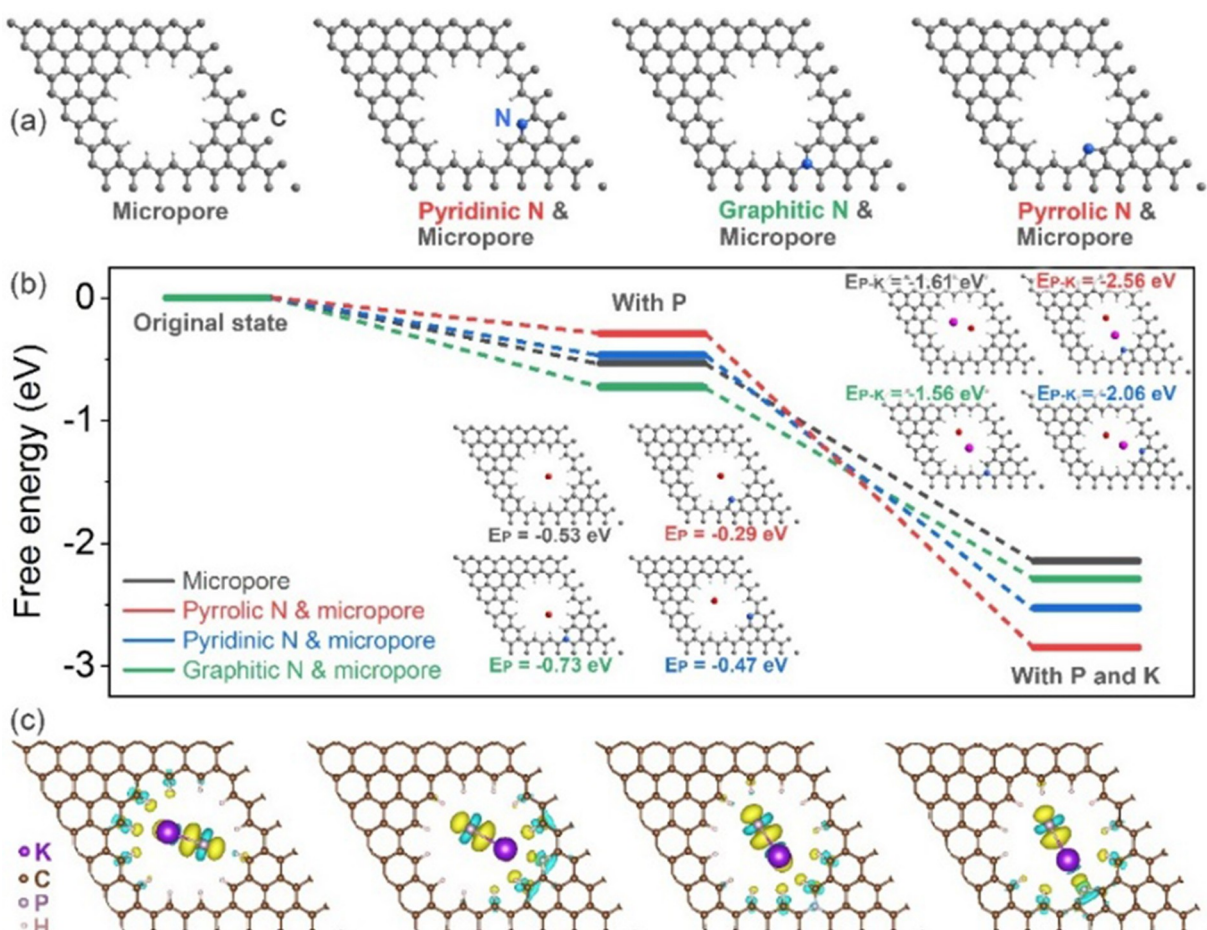


**Figure 4.** a) Schematic illustrations of four kinds of microporous carbon models. b) Free energy profiles of four kinds of carbon models after the stepwise introduction of phosphorus and potassium atoms. c) Charge density difference of four kinds of carbon models incorporated with both phosphorus and potassium atoms. Yellow and blue areas represent electron accumulation and depletion, respectively.

ment ability to promotionally confine red phosphorus (Figure 4b). Moreover, it was found that the nitrogen doping can promote the subsequent potassium storage into the phosphorus-incorporated carbon models, with free energy change of  $-2.56$ ,  $-1.56$ , and  $-2.06$  eV for those models with pyrrolic, graphitic, and pyridinic nitrogen doping, respectively, much lower than that of pure carbon model ( $-1.61$  eV). The charge density difference profiles of the models after phosphorus incorporation and potassium storage displayed large strong charge redistribution between potassium, phosphorus, and the carbon models, which indicated strong interactions between these components (Figure 4c). These calculation results demonstrated that both the micropores and the nitrogen doping played important role on the potassium storage performance. The micropores can efficiently confine phosphorus while the nitrogen doping can greatly promote the reaction between phosphorus and potassium, which together rendered P@NCS-75 with high rate capability and high cycling stability.

The role of the nanorod-assembled superstructure was also verified. Nitrogen-doped carbon nanorod without superstruc-

ture (NC) was fabricated by using Al-MOF nanorod as a precursor (Figure S7). The resultant P@NC exhibited a specific capacity close to that of P@NCS-75 at low current density but a much lower capacity of only  $136 \text{ mAh g}^{-1}$  at current density of  $8 \text{ A g}^{-1}$ . The superior potassium storage performance of P@NCS-75 over P@NC was contributed to the nanorod-assembled superstructure, which can provide interconnected channels and pathways for fast electron/mass transport. This conclusion was also confirmed by EIS measurements, where the Nyquist profile of P@NCS-75 showed a much smaller radius than that of P@NC-75 (Figure S8).

A potassium-ion full cell was assembled using P@NCS-75 and PTCDA as anode and cathode materials, respectively (Figure 5a). The PTCDA has a reversible specific capacity of  $152 \text{ mAh g}^{-1}$  with charge/discharge voltage platforms within 2–3 V (Figure 5b). Several charge-discharge cycles were carried out for both P@NCS-75 and PTCDA before assembling the full cell in order to prevent irreversible capacity loss. The assembled full cell exhibited a maximum working voltage higher than 3 V and a voltage platform at about 2 V, which were consistent with the half-cell measurements. A high specific capacity of

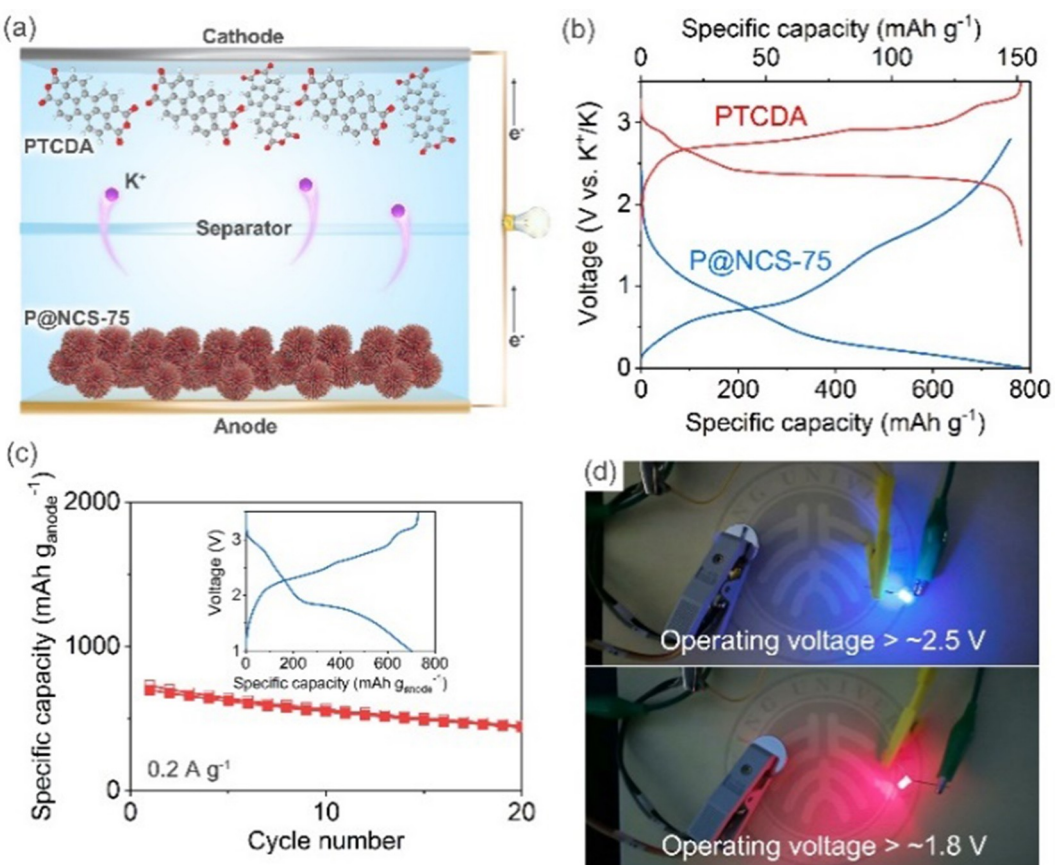


**Figure 5.** a) Schematic illustration of the potassium-ion full cell with P@NCS-75 and PTCDA as anode and cathode materials, respectively. b) GCD profiles of P@NCS-75 and PTCDA at current density of 0.1 A g<sup>-1</sup>. c) Cycling performance of the resultant full cell at 0.2 A g<sup>-1</sup>. Insert displayed the GCD profiles of the full cell. d) Digital photographs of the blue and red LEDs lighted by the full cell.

about 700 mAh g<sup>-1</sup> was delivered based on the weight of anode material. The fully charged full cell was able to light a blue LED (operating voltage > 2.5 V) and a red LED (operating voltage > 1.8 V), suggesting the practical applicability of P@NCS-75 for PIBs.

### 3. Conclusions

In conclusion, we presented a nitrogen-doped microporous carbon superstructure as an efficient substrate to confine red phosphorus components for electrochemical potassium storage with high specific capacity, high rate capability, and high cycling stability. Control experiments and theoretical calculations demonstrated that the nitrogen-modified micropores can efficiently confine phosphorus and promote its reaction with potassium. Also, the nanorod-assembled superstructure can facilitate the electron and mass transport as well as buffer the volume change of phosphorus. A potassium-ion full cell was assembled to light LEDs, revealing the great potential of the presented phosphorus composite for practical PIBs. This work not only provided a high-performance anode material for PIBs, but also offer guidance to improve the rate capability and

cycling stability of phosphorus-based material for electrochemical energy storage applications.

### Acknowledgements

This work was financially supported by the National Key Research and Development Program of China (2020YFA0210701), the National Natural Science Foundation of China (51825201, 52102199).

### Conflict of Interest

The authors declare no conflict of interest.

**Keywords:** carbon superstructure · metal-organic frameworks · potassium storage · red phosphorous

- [1] B. Dunn, H. Kamath, J.-M. Tarascon, *Science* 2011, 334, 928–935.
- [2] E. Pomerantseva, F. Bonaccorso, X. Feng, Y. Cui, Y. Gogotsi, *Science* 2019, 366, 969.

- [3] D. H. S. Tan, A. Banerjee, Z. Chen, Y. S. Meng, *Nat. Nanotechnol.* **2020**, *15*, 170–180.
- [4] F. Wu, J. Maier, Y. Yu, *Chem. Soc. Rev.* **2020**, *49*, 1569–1614.
- [5] T. Liu, Y. Zhang, Z. Jiang, X. Zeng, J. Ji, Z. Li, X. Gao, M. Sun, Z. Lin, M. Ling, J. Zheng, C. Liang, *Energy Environ. Sci.* **2019**, *12*, 1512–1533.
- [6] J. C. Pramudita, D. Sehrawat, D. Goonetilleke, N. Sharma, *Adv. Energy Mater.* **2017**, *7*, 1602911.
- [7] R. Rajagopalan, Y. Tang, X. Ji, C. Jia, H. Wang, *Adv. Funct. Mater.* **2020**, *30*, 1909486.
- [8] Y.-S. Xu, S.-Y. Duan, Y.-G. Sun, D.-S. Bin, X.-S. Tao, D. Zhang, Y. Liu, A.-M. Cao, L.-J. Wan, *J. Mater. Chem. A* **2019**, *7*, 4334–4352.
- [9] W. Zhang, Y. Liu, Z. Guo, *Sci. Adv.* **2019**, *5*, 7412.
- [10] Y. Li, Q. Zhang, Y. Yuan, H. Liu, C. Yang, Z. Lin, J. Lu, *Adv. Energy Mater.* **2020**, *10*, 2000717.
- [11] W.-C. Chang, J.-H. Wu, K.-T. Chen, H.-Y. Tuan, *Adv. Sci.* **2019**, *6*, 1801354.
- [12] Y. Xu, J. Zhang, D. Li, *Chem. Asian J.* **2020**, *15*, 1648–1659.
- [13] K.-X. Lei, J. Wang, C. Chen, S.-Y. Li, S.-W. Wang, S.-J. Zheng, F.-J. Li, *Rare Met.* **2020**, *39*, 989–1004.
- [14] S.-H. Qi, J.-W. Deng, W.-C. Zhang, Y.-Z. Feng, J.-M. Ma, *Rare Met.* **2020**, *39*, 970–988.
- [15] K. Song, C. Liu, L. Mi, S. Chou, W. Chen, C. Shen, *Small* **2021**, *17*, 1903194.
- [16] D. Liu, X. Huang, D. Qu, D. Zheng, G. Wang, J. Harris, J. Si, T. Ding, J. Chen, D. Qu, *Nano Energy* **2018**, *52*, 1–10.
- [17] Y. Wu, S. Hu, R. Xu, J. Wang, Z. Peng, Q. Zhang, Y. Yu, *Nano Lett.* **2019**, *19*, 1351–1358.
- [18] W. Li, S. Hu, X. Luo, Z. Li, X. Sun, M. Li, F. Liu, Y. Yu, *Adv. Mater.* **2017**, *29*, 1605820–1605828.
- [19] W. Xiao, X. Li, B. Cao, G. Huang, C. Xie, J. Qin, H. Yang, J. Wang, X. Sun, *Nano Energy* **2021**, *83*, 105772.
- [20] H. Wang, L. Wang, L. Wang, Z. Xing, X. Wu, W. Zhao, X. Qi, Z. Ju, Q. Zhuang, *Chem. Eur. J.* **2018**, *24*, 13897–13902.
- [21] J. Zhao, X. Zou, Y. Zhu, Y. Xu, C. Wang, *Adv. Funct. Mater.* **2016**, *26*, 8103–8110.
- [22] Z. Jian, W. Luo, X. Ji, *J. Am. Chem. Soc.* **2015**, *137*, 11566–11569.
- [23] W. Luo, J. Wan, B. Ozdemir, W. Bao, Y. Chen, J. Dai, H. Lin, Y. Xu, F. Gu, V. Barone, L. Hu, *Nano Lett.* **2015**, *15*, 7671–7677.
- [24] Y. Xu, C. Zhang, M. Zhou, Q. Fu, C. Zhao, M. Wu, Y. Lei, *Nat. Commun.* **2018**, *9*, 1720.
- [25] J. Chen, B. Yang, H. Hou, H. Li, L. Liu, L. Zhang, X. Yan, *Adv. Energy Mater.* **2019**, *9*, 1803894.
- [26] H. He, D. Huang, Y. Tang, Q. Wang, X. Ji, H. Wang, Z. Guo, *Nano Energy* **2019**, *57*, 728–736.
- [27] C. Lv, W. Xu, H. Liu, L. Zhang, S. Chen, X. Yang, X. Xu, D. Yang, *Small* **2019**, *15*, 1900816.
- [28] Z. Liang, Y. Wu, J. Cheng, Y. Tang, J. Shi, T. Qiu, W. Li, S. Gao, R. Zhong, R. Zou, *Small* **2021**, *17*, 2100135.
- [29] W. Yang, J. Zhou, S. Wang, Z. Wang, F. Lv, W. Zhang, W. Zhang, Q. Sun, S. Guo, *ACS Energy Lett.* **2020**, *5*, 1653–1661.
- [30] Y. Wu, Z. Liu, X. Zhong, X. Cheng, Z. Fan, Y. Yu, *Small* **2018**, *14*, 1703472.

Manuscript received: September 18, 2021

Revised manuscript received: October 29, 2021

Accepted manuscript online: November 3, 2021

Version of record online: November 17, 2021